*Korean J. Chem. Eng.*, 39(5), 1232-1239 (2022)
DOI: 10.1007/s11814-021-1041-8

pISSN: 0256-1115
eISSN: 1975-7220

# Preparation and electrochemical characterization of porous carbon pearls from carboxymethyl cellulose for electrical double-layer capacitors

**Hyeong Seok Chang*,‡, Byoung-Min Lee*,‡, Je Moon Yun**,†, and Jae-Hak Choi*,†**

*Department of Polymer Science and Engineering, Chungnam National University, 99 Daehak-ro, Yuseong-gu, Daejeon 34134, Korea
**Division of Advanced Materials Engineering, Dong-Eui University, 176 Eongwang-no, Busanjin-gu, Busan 47340, Korea
(*Received 5 October 2021 • Revised 1 December 2021 • Accepted 13 December 2021*)

**Abstract**−Porous carbon pearls (PCPs) were successfully prepared from syringe droplets of highly concentrated carboxymethyl cellulose solution via ice-templating followed by carbonization. The PCPs, which look like a solid bead with a pearly luster, were found to have well-developed bi-modal pore structures with a large specific surface area of 1,338.6 $m^2$/g and a total pore volume of 0.81 $cm^3$/g (a mesopore volume of 0.28 $cm^3$/g and a micropore pore volume of 0.53 $cm^3$/g). In a three-electrode system, the PCPs-based electrode exhibited high supercapacitive performance, such as a high specific capacitance of 217 F/g at 1 A/g in 6 M aqueous KOH electrolyte, outstanding cycling stability of 100% after 10,000 cycles at 30 A/g, and excellent rate capability of 63.7%. To investigate actual supercapacitive performance, a symmetric capacitor device was assembled using a coin cell. The PCPs-based device showed a specific capacitance of 37 F/g at a current density of 1 A/g and a power density of 5.0 kW/kg at an energy density of 2.88 Wh/kg. Furthermore, the PCPs-based device also exhibited superior cycling stability with capacitance retention of 98.5% after 10,000 cycles at a current density of 10 A/g.

Keywords: Porous Carbon Pearl, Ice-templating, Electric Double-layer Capacitor, Carboxymethyl Cellulose, Carbonization

## INTRODUCTION

Electrical double-layer capacitors (EDLCs) have been widely used as a power source in various applications, such as electronic devices, electric vehicles, and memory backup, due to their high power density, high charge/discharge ratio, semi-permanent lifetime, and stable operation ability [1]. EDLCs store energy based on an electrical double-layer mechanism, namely, the physical adsorption/desorption of electrolyte ions on the electrode surface [2,3]. Therefore, the large specific surface area (SSA) and well-developed pore structures of the electrode are essential factors in determining the electro-chemical performance of EDLCs [4,5]. Activated carbon (AC) has been generally used as an active material for the electrode of EDLCs due to its large SSA and low cost. However, the low electrical conductivity of AC increases the internal resistance of EDLCs. In addition, although AC has a large surface area, the low content of meso- and micro-pores in AC hinders the accessibility of electrolyte ions on the electrode surface [2-6].

Various types of porous carbon materials (PCMs) have been developed as active materials in EDLC applications to overcome the drawbacks of AC [7]. Among various PCMs, spherical porous carbon pearls (PCPs) have been reported. Lee et al. synthesized PCPs via non-solvent-induced phase separation, carbonization, and activation using polyacrylonitrile (PAN). The PCPs showed an SSA of 1,147.99 $m^2$/g, a specific capacitance of 112 F/g at 1 A/g, and cycling stability of 100% after 10,000 cycles [8]. Shu et al. reported that PCPs with an SSA of 2,900 $m^2$/g were synthesized from resorcinol-formaldehyde (RF) resin via emulsion polymerization, hydrothermal treatment, carbonization, and activation. The PCPs showed the specific capacitance of 168 F/g at 2 mV/s and cycling stability of 95% after 5,000 cycles, respectively [9]. Lee et al. synthesized PCPs from polystyrene (PS) by emulsion polymerization, carbonization, and nitrogen doping. The nano-sized PCPs exhibited a specific capacitance of 191.9 F/g at 0.1 A/g and cycling stability of 110% after 10,000 cycles at 1 A/g [10]. Chen et al. reported that PCPs prepared from sodium lignosulphonate by spray drying and activation/carbonization showed an SSA of 1,372.87 $m^2$/g and a specific capacitance of 340 F/g at 0.5 A/g [11].

In this study, we report a simple and effective method to prepare rigid PCPs from syringe droplets of highly concentrated carboxymethyl cellulose (CMC) solution by ice-templating and carbonization. CMC is a non-toxic, biocompatible, eco-friendly, sustainable, and water-soluble polysaccharide [12,13]. CMC pearls (CPs) were fabricated by the direct addition of syringe droplets of an aqueous CMC solution to a liquid $N_2$ bath. PCPs were finally obtained by the carbonization of the CPs. The PCPs were characterized in terms of their morphology, chemical structure, pore structure and electrochemical performance.

## EXPERIMENTAL SECTION

### 1. Materials

CMC (Na salt, Mw: 90,000, DS: 0.7) was purchased from Sigma-

†To whom correspondence should be addressed.
E-mail: jmyun@deu.ac.kr, jaehakchoi@cnu.ac.kr
‡These authors contributed equally to this work.

Aldrich. Carbon black (Super-P conductive, 99+%, Alfa Aesar) and polytetrafluoroethylene (PTFE, 60 wt% dispersion in $H_2O$, Sigma-Aldrich) were used as a conductive material and a binder, respectively.

**2. Preparation of PCPs**

PCPs were prepared from CMC by ecofriendly ice-templating followed by carbonization. Briefly, an aqueous CMC solution (CMC of 4, 8, and max. 16 g in 200 mL of DI water) was added dropwise with a dropping rate of 15 mL/h to a liquid $N_2$ bath using a syringe pump and then dried in a freeze dryer (FD 8512, IlShin-BioBase, Korea) at −85 °C for three days under 5 mTorr to obtain CPs. The CPs were carbonized at 1,000 °C (heating rate: 5 °C/min) for 1 h in a tubular furnace (Youlsan, Korea) under high purity $N_2$ atmosphere (500 sccm). After carbonization, the PCPs were washed using 1 M HCl and DI water several times to remove the residual sodium and then dried. The carbonization yield calculated by the weight ratio of the PCPs to CPs was about 23%. The obtained CPs and PCPs samples were named as CPs-x and PCPs-x, respectively, where x is the initial CMC amount (4 g, 8 g, and 16 g) in 200 mL of DI water.

**3. Characterization**

The morphology was observed by field-emission scanning electron microscopy (FE-SEM, UHR SU8230, Hitachi, Japan) after the Pt coating. Raman spectra were obtained using a high-resolution Raman spectrometer (LabRam HR-800, Horiba, Japan) with an exciting laser wavelength of 514 nm. X-ray diffraction (XRD) patterns were obtained by using an X-ray diffractometer (X'Pert Pro Multi-Purpose, PANalytical, Netherlands) with CuK$\alpha$ radiation at a range of $2\theta$=10 to 60°. The changes in the chemical structure and composition were investigated by X-ray photoelectron spectrometry (XPS, Multi-Lab 2000, Thermo Electron Corp., England). The $N_2$ adsorption/desorption measurement was carried out at 77 K using a surface area analyzer (NanoPorosity-XQ, Mirae Scientific Instruments, Korea). The PCPs samples were outgassed under high vacuum ($10^{-6}$ mbar) at 150 °C for 12 h. The SSA and pore volume were analyzed using Brunauer-Emmett-Teller (BET) and Barrett-Joyner-Halenda (BJH) methods, respectively. The micro-pore area and volume were analyzed by Horvath-Kawazoe (HK) method. The compressive strength of the PCPs-16 was measured with a micro material tester (Instron 5848, England).

**4. Electrochemical Measurements**

The working electrodes were composed of the PCPs (active material), carbon black (conductive material), and PTFE (binder). A slurry of the PCPs, carbon black, and PTFE at a ratio of 8 : 1 : 1 in DI water was coated on the Ni foam and then dried at 70 °C for 5 h. The loading level of the active material was 2.4 mg. Hg/HgO and Pt mesh were used as reference and counter electrodes, respectively. The electrochemical measurements were performed using an electrochemical workstation (MP2A Electrochemical Workstation, WonA Tech, Korea) with a three-electrode system in a 6 M aqueous KOH electrolyte. Cyclic voltammetry (CV) curves were recorded at a scan rate of 10 to 50 mV/s at a potential window from −1.0 to 0 V. Galvanostatic charging/discharging (GCD) tests were performed at a current density of 1 to 30 A/g at a potential window from −1.0 to 0 V. Electrochemical impedance spectroscopy (EIS) spectra were obtained with a signal amplitude of 10 mV at a frequency range of 0.01 to 100,000 Hz. The specific capacitance (C) was calculated as:

$$C = \frac{I \times \Delta t}{m \times \Delta V} \quad (1)$$

where C is in F/g, I is the discharge current (A), Δt is the discharge time (s), m is the mass of the active material (g) of the electrode, and ΔV is the potential window (V).

A symmetric supercapacitor was assembled using the same two PCPs-based electrodes with an active material loading of 4 mg. Cellulose filter paper (Whatman filter No. 4) and 6 M KOH aqueous solution were used as a separator and an electrolyte, respectively. CV and GCD tests were performed in a potential window 0 to 1 V at a scan rate of 10 to 50 mV/s and at a current density of 1 to 10 A/g, respectively. The specific capacitance was calculated by using Eq. (1). The energy density (E, Wh/kg) and power density (P, W/kg) were determined by using the following equations:

$$E = \frac{C \times (\Delta V)^2}{2 \times 3.6} \quad (2)$$

$$P = \frac{3{,}600 \times E}{\Delta t} \quad (3)$$

## RESULTS AND DISCUSSION

**1. Morphological Investigation**

The preparation of PCPs from CMC by ice-templating followed by carbonization is presented in Fig. 1(a). The morphology of CPs and PCPs was observed by digital and FE-SEM images, and the results are shown in Fig. 1(b)-(d). As seen in Fig. 1(b), although the average diameter of the CPs decreased from 3.5 to 1.5 mm after carbonization, the spherical shapes were well preserved. As seen in Fig. 1(c), all of the CPs samples show radially aligned micro-channels formed during ice-templating and freeze-drying. The CPs-4 and CPs-8 show distorted shapes by their cross-section cut using a sharp knife due to the poor mechanical integrity caused by the low concentration of CMC. The CPs obtained at a low CMC concentration show bigger channel size compared to the sample obtained at a higher CMC concentration. After carbonization, as seen in Fig. 1(d), more wrinkles and smaller pores were formed on the walls of the channels with increasing the CMC concentration. These results indicate the critical role of the CMC concentration in the preparation of CPs with good mechanical integrity and pore structures. In addition, the PCPs-16 prepared from the CPs-16 with the highest concentration exhibited a high compressive strength of about 11.85 MPa, which was much higher than that of porous carbon spheres published in the literature [14].

**2. Physical and Chemical Structure**

Raman and XRD analyses were conducted to investigate the carbon and crystalline structure. Fig. 2(a) shows the XRD patterns of the CMC and PCPs samples. The characteristic peak at $2\theta$=19° corresponds to the amorphous structure of CMC [15]. For the PCPs samples, the broad peaks newly appearing at $2\theta$=24° and 43° correspond to the (002) and (100) planes of the amorphous carbon structure, respectively [16]. As seen in Fig. 2(b), the Raman spectra show two peaks at 1,340 $cm^{-1}$ (D-band) and 1,580 $cm^{-1}$ (G-band),

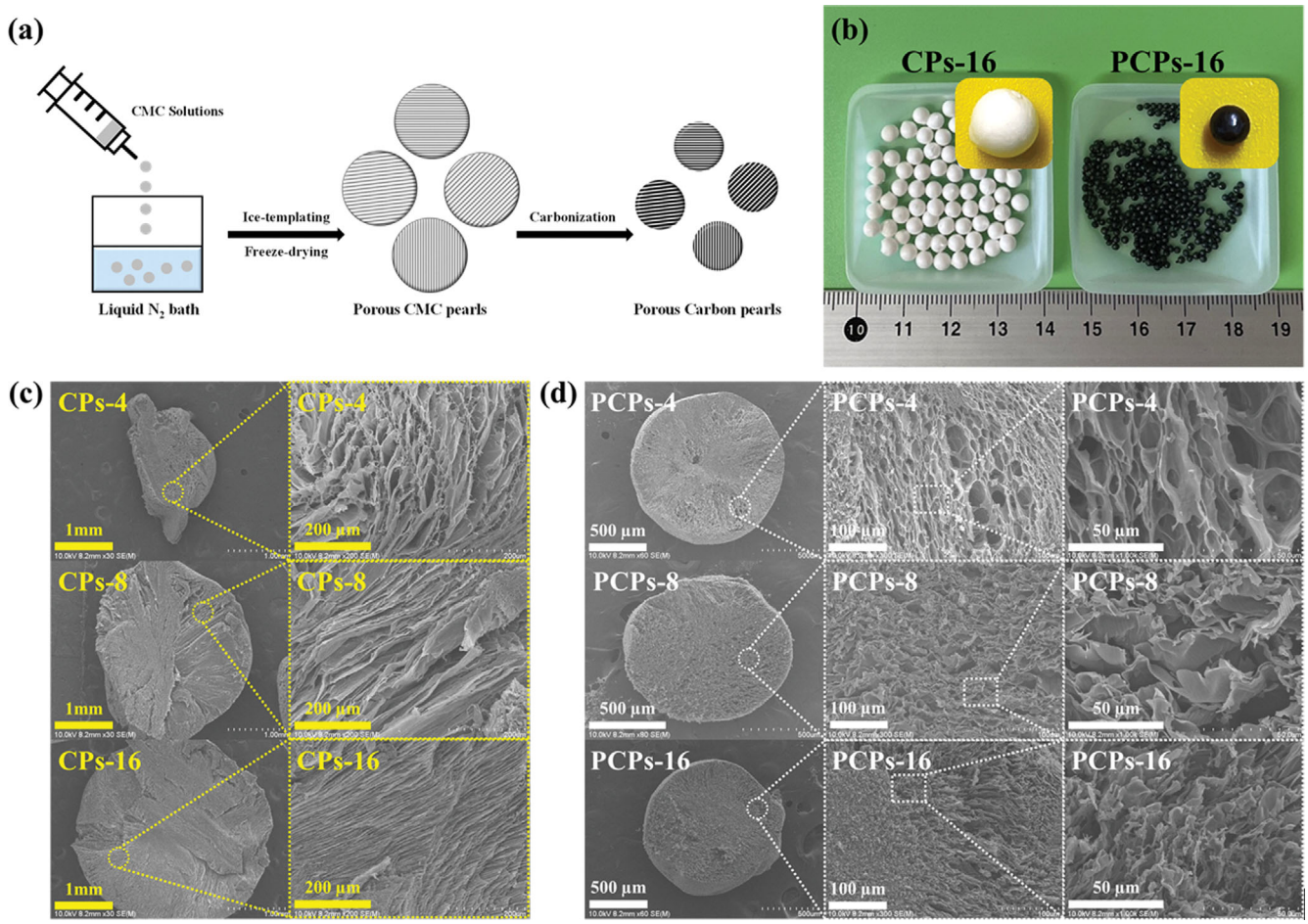


**Fig. 1. (a) Schematic illustration for the preparation of PCPs, (b) digital images of CPs and PCPs with each magnification, (c)-(d) FE-SEM images of CPs-4, CPs-8, CPs-16, PCPs-4, PCPs-8, and PCPs-16.**

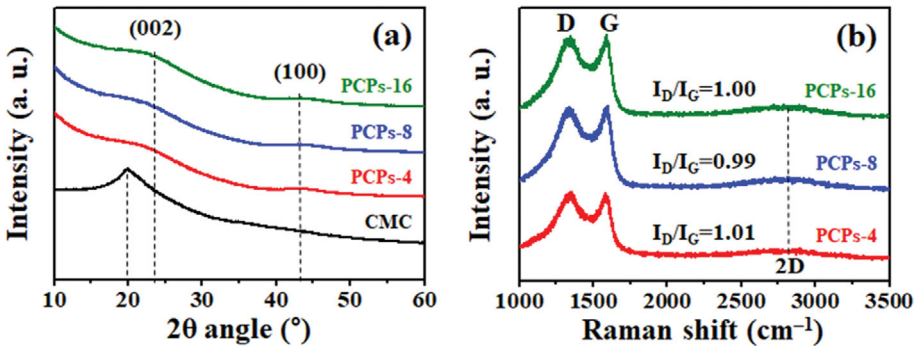


**Fig. 2. (a) XRD patterns of CMC, PCPs-4, PCPs-8, and PCPs-16; (b) Raman spectra of PCPs-4, PCPs-8, and PCPs-16.**

respectively. The D-band is due to the disordered carbon structure, while the G-band corresponds to the sp2-hybridized carbon structure. The relative intensity ratio ($I_D/I_G$) of the PCPs is in the rage of 0.99 to 1.01, indicating that the PCPs have amorphous carbon structure with a low degree of graphitization [17].

XPS analysis was performed to investigate the change in the elemental composition and chemical structure. In Fig. 3(a), the XPS survey spectrum of CMC shows C, O, and Na elements located at 285, 532, and 1,070 eV, respectively, and the atomic percentages were 53.45% (C), 40.95% (O), and 5.6% (Na), respectively [15]. After carbonization (PCPs-16), the C content increased to 90.82%, while the O content decreased to 9.18%. Moreover, the atomic ratio of the O and C atoms ([O]/[C]) of the PCPs decreased to 0.1 due to the removal of non-carbon elements during carbonization. The XPS narrow spectra were deconvoluted to investigate the change in the chemical structure before and after carbonization. In Fig. 3(b), CMC shows the characteristic peaks of C=O, C-O-C, and C-C at 287.5, 286, and 284 eV, respectively. In the case of the PCPs-

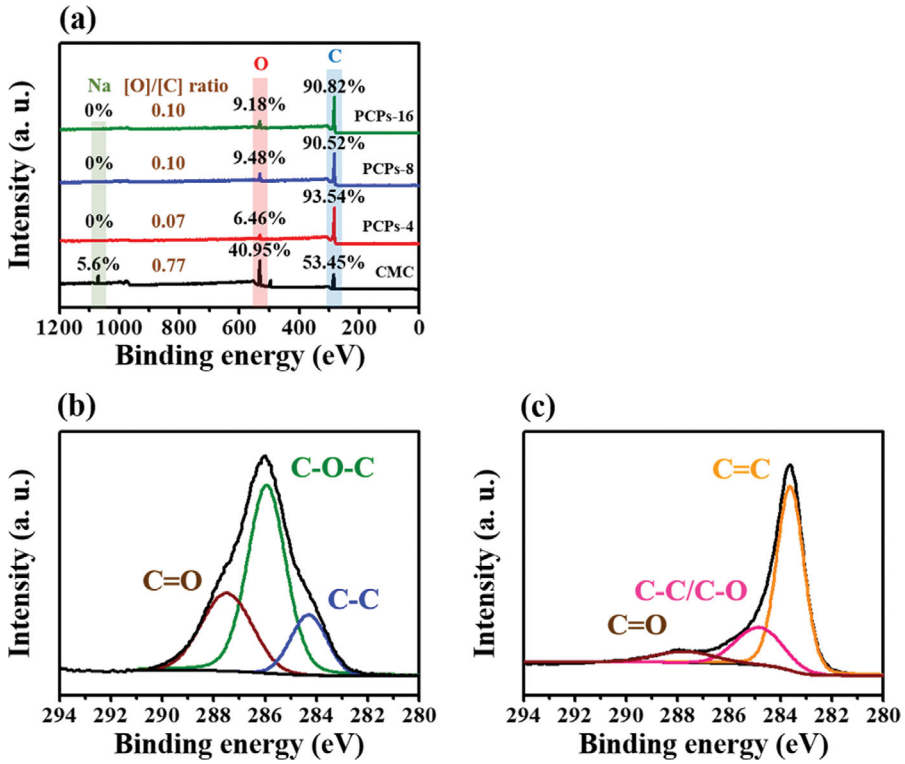


**Fig. 3. (a) XPS survey spectra of CMC, PCPs-4, PCPs-8, and PCPs-16; C1s narrow spectra of (b) CMC and (c) PCPs-16.**

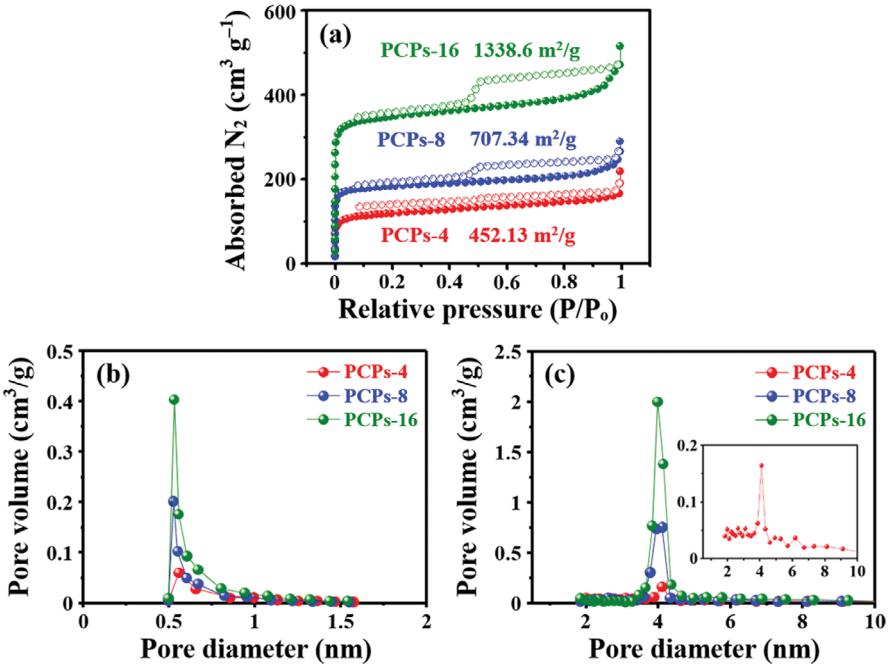


**Fig. 4. (a) $N_2$ isotherms, (b) micro-pore size distribution, and (c) meso-pore size distribution of PCPs samples.**

16 (Fig. 3(c)), the peak intensity for C=O (287.5 eV) decreased, while the peaks for C-O (284.8 eV) and C=C (283.5 eV) newly appeared due to the formation of conjugated and graphite-like structure, respectively. These results indicate that a graphite-like carbon structure was formed after carbonization [18].

### 3. Pore Structure

$N_2$ adsorption/desorption tests were performed to investigate the pore structure of the PCPs samples (Fig. 4 and Table 1). As shown in Fig. 4(a), all the PCPs samples showed $N_2$ adsorption at a relative pressure ($P/P_o$) of <0.1, indicating the presence of plentiful micro-

**Table 1. The pore properties of the PCPs samples**

| Sample | SSA ($m^2/g$) | Mean mesopore diameter (nm) | Total pore volume ($cm^3/g$) | BJH pore volume ($cm^3/g$) | Micropore volume ($cm^3/g$) | BJH pore area ($m^2/g$) | Micropore area ($m^2/g$) |
|---|---|---|---|---|---|---|---|
| PCPs-4 | 452.13 | 3.37 | 0.26 | 0.09 | 0.17 | 87.99 | 333.6 |
| PCPs-8 | 707.34 | 3.528 | 0.44 | 0.17 | 0.27 | 145.59 | 574.42 |
| PCPs-16 | 1,338.6 | 3.594 | 0.80 | 0.28 | 0.52 | 259.3 | 1,099.2 |

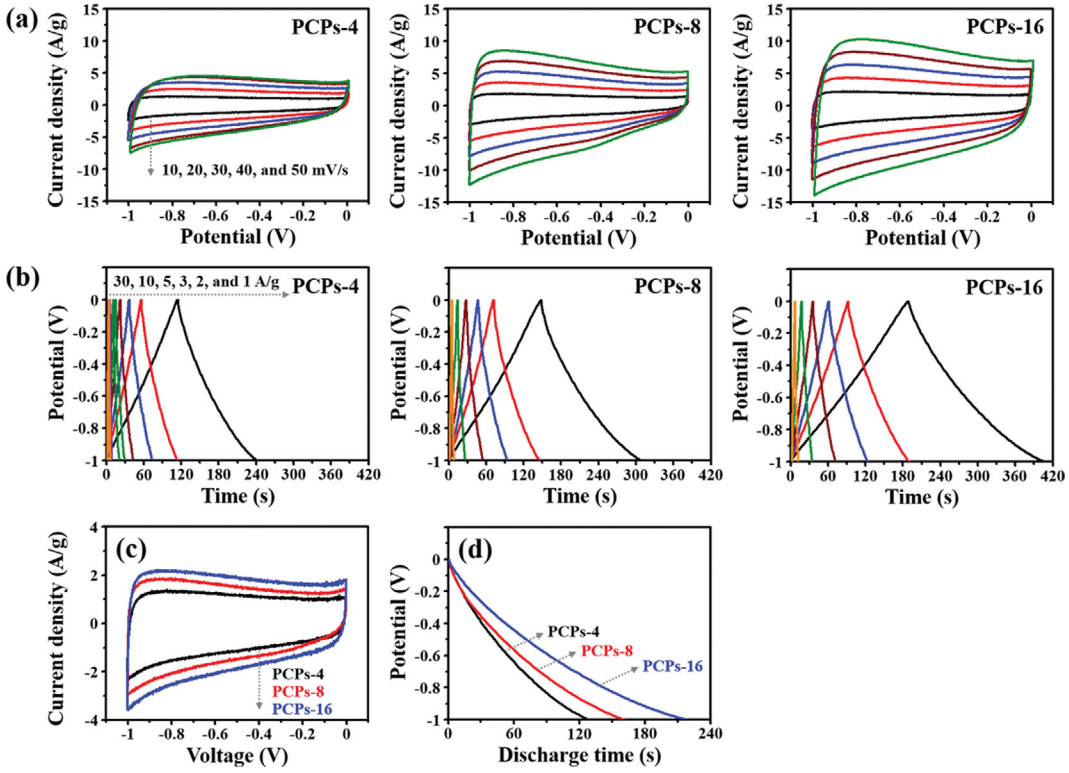


**Fig. 5. (a) CV curves, (b) GCD curves, (c) CV curves at a scan rate of 10 mV/s, and (d) discharge times of PCPs-4, PCPs-8, and PCPs-16 at a current density of 1 A/g.**

pores [19]. At $P/P_o$ ranging from 0.4 to 0.9, type-IV isotherms with a hysteresis loop were observed, indicating the presence of meso-pores [20]. Based on these results, we confirmed that the PCPs samples have bi-modal pore structure. As seen in Table 1, the SSA, total pore volume, BJH pore volume, and micro-pore volume of the PCPs increased to 1,338.6 $m^2/g$, 0.58 $cm^3/g$, 0.28 $cm^3/g$, and 0.30 $cm^3/g$, respectively, with an increase in the concentration of CMC. The BJH pore area and micro-pore area also increased to 259.3 and 1,099.2 $m^2/g$ with an increase in the CMC concentration. Furthermore, the PCPs-16 sample shows a mean meso-pore diameter of 3.594 nm. Based on these results, the PCPs-16 sample with the largest SSA and highest pore diameter and pore volume can be expected to have the highest EDLC performance, such as high capacitance, easy ion transport, and fast ion diffusion [21,22].

**4. Electrochemical Performance**

The CV curves of the PCPs-based electrodes shown in Fig. 5(a) were obtained with various scan rates (10 to 50 mV/s) at a potential window of −1.0 to 0 V. As the scan rate was increased, the current density range and area in the CV curves widened without any distortion. Furthermore, the CV curves show the electrostatic adsorption/desorption of electrolyte ions without a redox peak, indicating that the PCPs-based electrodes show typical EDLC capacitive behavior [23]. The PCPs-16 shows the largest integral area of the CV curve at the same current density, indicating that the PCPs-16-based electrode has the largest specific capacitance (Fig. 5(c)) [24]. The GCD curves of the PCPs-based electrodes were obtained at various current densities of 1 to 30 A/g in a potential window of −1.0 to 0 V, and the results are shown in Fig. 5(b). The GCD curves of all the PCPs-based electrodes show a triangular shape. The discharge time increased in the order of PCPs-16>PCPs-8>PCPs-4 (Fig. 5(d)), indicating that the PCPs-16-based electrode has the highest specific capacitance [25]. These results are consistent with the results of the pore properties.

The specific capacitance of all the PCPs-based electrodes was calculated at current density of 1 to 30 A/g (Fig. 6(a)). The PCPs-16-based electrode showed the highest specific capacitance of 217 F/g at 1 A/g and 138 F/g at 30 A/g, respectively. The rate capability of the PCPs-16-based electrode at a high current density of 30 A/g was 63.7%, indicating the bi-modal pore structure and good electrical conductivity of the PCPs-16 [26]. These results suggest that

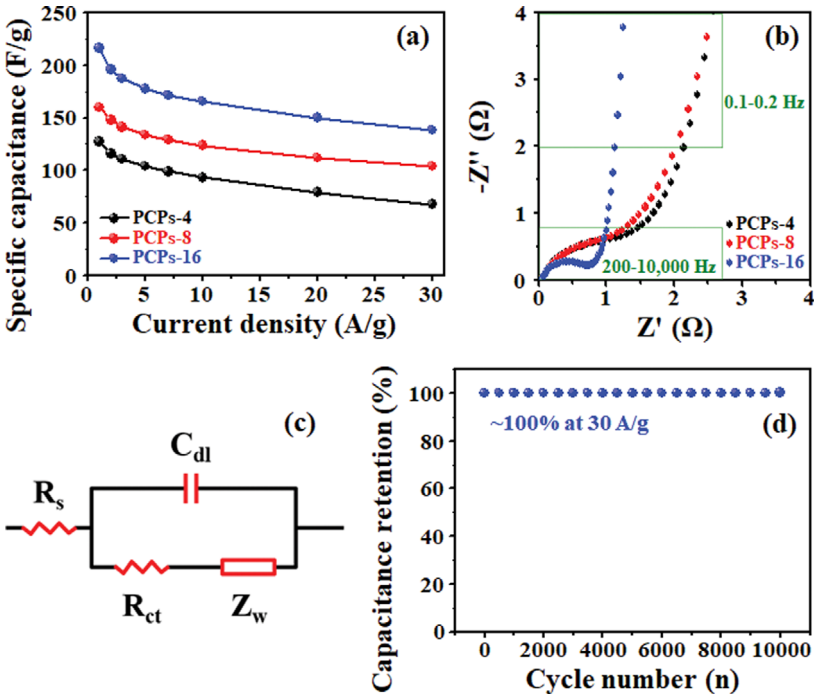


**Fig. 6. (a) Specific capacitance at various current densities and (b) Nyquist plots of PCPs-4, PCPs-8, and PCPs-16; (c) equivalent circuit model; and (d) capacitance retention of PCPs-16.**

PCPs-16 is promising as an electrode material for high-performance EDLCs. As seen in Fig. 6(b)-(c), the electrical properties of the PCPs were evaluated through an EIS test. The Nyquist plot of the PCPs-16-based electrode exhibits the smallest semicircle at a high frequency and a nearly vertical line at a low frequency compared to the PCPs-4 and PCPs-8, indicating the better EDLC capacitive properties of the PCPs-16-based electrode, such as low internal resistance ($R_s$, 0.06 Ω) and low charge transfer resistance ($R_{ct}$, 0.71 Ω) (Table 2) [27]. As seen in Fig. 6(d), the cycle retention of the PCPs-16-based electrode at a high current density of 30 A/g shows outstanding capacitance retention of 100% after 10,000 cycles, indicating that the PCPs-16-based electrode has high electrochemical stability and durability. The electrochemical performance of the PCPs-16-based electrode was comparable to other PCMs-based supercapacitors (Table 3). These results reveal that the PCPs-16 is promising as an electrode material for high-performance EDLCs.

**Table 2. $R_s$ and $R_{ct}$ values of PCPs samples**

| Sample | $R_s$ (Ω) | $R_{ct}$ (Ω) |
|---|---|---|
| PCPs-4 | 0.05 | 1.17 |
| PCPs-8 | 0.05 | 1.10 |
| PCPs-16 | 0.06 | 0.71 |

**Table 3. Electrochemical performance of various PCPs using a three-electrode system**

| PCPs | Carbon precursor | Method | SSA ($m^2$/g) | Specific capacitance (F/g) | Retention | Reference |
|---|---|---|---|---|---|---|
| PCPs | Carboxymethyl cellulose | Ice-templating and carbonization | 1,338.6 | 217 @1 A/g | 100% (10,000 cycles) | This work |
| Activated PCPs | Polyacrylonitrile | Non-solvent induced phase separation, carbonization, and activation | 1,147.99 | 112 @1 A/g | 100% (10,000 cycles) | [8] |
| Activated PCPs | Resorcinol formaldehyde | Emulsion polymerization, hydrothermal treatment, carbonization, and activation | 2,900 | 168 @2 mV/s | 95% (5,000 cycles) | [9] |
| N-doped PCPs | Polystyrene | Emulsion polymerization, carbonization, and N-doping | 145.48 | 191.9 @0.1 A/g | 110% (10,000 cycles) | [10] |
| Activated PCPs | Sodium lignosulphonate | Spray drying and activation/carbonization | 1,372.87 | 340 @0.5 A/g | - | [11] |

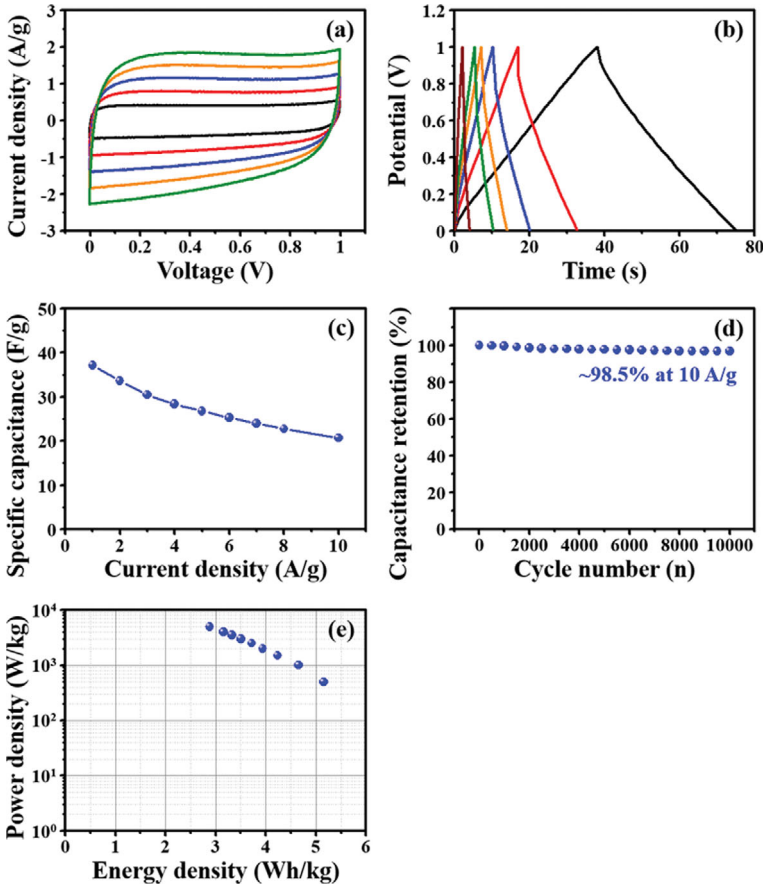


**Fig. 7. (a) CV curves at 10, 20, 30, 40, and 50 mV/s, (b) GCD curves at 1, 2, 3, 4, 5, and 10 A/g, (c) specific capacitance at 1 to 10 A/g, (d) cycling stability, and (e) Ragone plot of the PCP-16-based symmetric device.**

To further investigate the actual supercapacitive behavior of PCPs-16-based electrodes, the electrochemical performance of a symmetrical two-electrode device with 6 M KOH electrolyte in a 2032 coin cell was tested. Fig. 7(a) shows CV curves at a voltage window of 0 to 1 V at scan rate of 10 to 50 mV/s. The CV curves exhibit ideal EDLC behavior with a rectangular shape that is well-maintained even at a higher scan rate of 50 mV/s. As seen in Fig. 7(b), the GCD curves at various current densities from 1 to 10 A/g exhibit triangular-shapes. The specific capacitance calculated from the GCD curves is shown in Fig. 7(c). The specific capacitance and rate capability were 37 F/g at a current density of 1 A/g and 55.7% at 10 A/g, respectively. In addition, the PCPs-16-based electrode exhibits an outstanding cycling stability of 98.5% after 10,000 cycles at 10 A/g (Fig. 7(d)). As can be seen in the Ragone plot (Fig. 7(e)), the PCPs-16-based device exhibits high power density of 5.0 kW/kg at an energy density of 2.88 Wh/kg. Therefore, the PCPs-16 can be applied as an active material for high-performance supercapacitors.

## CONCLUSIONS

PCPs with a large SSA and well-developed bi-modal pore structures were prepared from a highly concentrated CMC solution by ice-templating followed by carbonization. The PCPs showed a well-defined spherical shape, uniform porous morphology, and amorphous carbon structure. The PCPs were found to have hierarchically dense pore structure containing evenly well-developed micro- and meso-pores. The PCPs-based electrode exhibited outstanding electrochemical performance, such as a high specific capacitance of 217 F/g at 1 A/g, high rate capability of 63.7% at 30 A/g, and outstanding cycle stability of ~100% after 10,000 cycles at 30 A/g. In addition, the symmetric device based on the PCPs-16 showed a high power density of 5.0 kW/kg at an energy density of 2.88 Wh/kg and superior cycling stability of 98.5% after 10,000 cycles. Therefore, the PCPs prepared in this study can be a promising candidate as an active material for the electrode of high-performance EDLCs.

## ACKNOWLEDGEMENTS

This work was supported by the Korea Institute of Energy Technology Evaluation and Planning (KETEP) grant funded by the Ministry of Trade, Industry & Energy (MOTIE) of the Republic of Korea (No. 20164010201070) and by the research fund of Chungnam National University.

## REFERENCES

1. J. Libich, J. Máca, J. Vondrák, O. Čech and M. Sedlaříková, *J. Energy Storage*, **17**, 224 (2018).

2. E. Fracowiak and F. Béguin, *Carbon*, **39**, 937 (2001).
3. L. L. Zhang and X. S. Zhao, *Chem. Soc. Rev.*, **38**, 2520 (2009).
4. Q. Wang, J. Yan, Y. Wang, T. Wei, M. Zhang, X. Jing and Z. Fan, *Carbon*, **67**, 119 (2014).
5. Y. Gao, Y. S. Zhou, M. Qian, X. N. He, J. Redepenning, P. Goodman, H. M. Li, L. Jiang and Y. F. Lu, *Carbon*, **51**, 52 (2013).
6. S. Song, F. Ma, G. Wu, D. Ma, W. Geng and J. Wan, *J. Mater. Chem. A*, **2**, 18154 (2015).
7. J. Yin, W. Zhang, N. A. Alhebshi, N. Salah and H. N. Alshareef, *Small Methods*, **4**, 1900853 (2020).
8. B. M. Lee, B. S. Choi, J. Y. Lee, S. K. Hong, J. S. Lee and J. H. Choi, *Carbon Lett.*, **31**, 67 (2021).
9. C. Zhang, K. B. Hatzell, M. Boota, B. Dyatkin, M. Beidaghi, D. Long, W. Qiao, E. C. Kumbur and Y. Gogotsi, *Carbon*, **77**, 155 (2014).
10. W. Lee and J. H. Moon, *ACS Appl. Mater. Interfaces*, **6**, 13968 (2014).
11. Y. Chen, G. Zhang, J. Zhang, H. Guo, X. Feng and Y. Chen, *J. Mater. Sci. Technol.*, **34**, 2189 (2018).
12. Y. Xu and Y. Zhang, *Mater. Lett.*, **139**, 145 (2015).
13. M. Yu, Y. Han, J. Li and L. Wang, *Chem. Eng. J.*, **324**, 287 (2017).
14. W. Yang, S. Mao, J. Yang, T. Shang, H. Song, J. Mabon, W. Swiech, J. R. Vance, Z. Yue, S. J. Dillon, H. Xu and B. Xu, *Sci. Rep.*, **6**, 24187 (2016).
15. B. M. Lee, C. U. Jeong, S. K. Hong, J. M. Yun and J. H. Choi, *J. Ind. Eng. Chem.*, **82**, 367 (2020).
16. B. M. Lee, H. G. Nam, H. Y. Choi, S. K. Hong, Y. G. Jeong and J. H. Choi, *Macromol. Mater. Eng.*, **303**, 1800296 (2018).
17. B. J. Koo, B. M. Lee, D. H. Kim, S. K. Hong, K. S. Go, E. H. Kwon, S. H. Kim, J. H. Choi and K. B. Lee, *ACS Appl. Mater. Interfaces*, **13**, 13106 (2021).
18. B. M. Lee, N. Umirov, J. Y. Lee, J. Y. Lee, B. S. Choi, S. K. Hong, S. S. Kim and J. H. Choi, *Int. J. Energy Res.*, **45**, 9530 (2021).
19. Y. Jiang, Y. Wang, D. Zeng, Y. Wang, Y. Ma, H. Wang, X. Zhang and X. Dai, *Dalton Trans.*, **48**, 4702 (2019).
20. M. Thommes, K. Kaneko, A. V. Neimark, J. P. Olivier, F. Rodriguez-Reinoso, J. Rouquerol and K. S. W. Sing, *Pure Appl. Chem.*, **87**, 1051 (2015).
21. L. Miao, H. Duan, Z. Wang, Y. Lv, W. Xiong, D. Zhu, L. Gan, L. Li and M. Liu, *Chem. Eng. J.*, **382**, 122945 (2020).
22. J. Pokrzywinski, J. K. Keum, R. E. Ruther, E. C. Self, M. Chi, H. Meyer, K. C. Littrell, D. Aulakh, S. Marble, J. Ding, M. Wriedt, J. Nanda and D. Mitlin, *J. Mater. Chem. A*, **5**, 13511 (2017).
23. Y. K. Lee, S. Chung, S. Y. Hwang, S. Lee, K. S. Eom, S. B. Hong, G. G. Park, B. J. Kim, J. J. Lee and H. I. Joh, *Korean J. Chem. Eng.*, **36**, 1543 (2019).
24. J. Yu, N. Fu, J. Zhao, R. Liu, F. Li, Y. Du and Z. Yang, *ACS Omega*, **4**, 15904 (2019).
25. L. Fan, P. Sun, L. Yang, Z. Xu and J. Han, *Korean J. Chem. Eng.*, **37**, 166 (2020).
26. S. Ghosh, W. D. Yong, E. M. Jin, S. R. Polaki, S. M. Jeong and H. Jun, *Korean J. Chem. Eng.*, **36**, 312 (2019).
27. Y. A. Kumar, K. D. Kumar and H. J. Kim, *Dalton Trans.*, **49**, 4050 (2020).